Sbalzarini et al. – Supplementary Material

Governing equation

Isotropic diffusion of a scalar quantity in the m-dimensional Euclidean space E^m ($m = 1, 2, 3$) is described by the spatio-temporal evolution of its local concentration $c(\boldsymbol{x}, t)$ on a given closed bounded domain $\Omega \subset E^m$ with boundary $\partial\Omega$ for a time interval $0 < t \leqslant T$. The governing equation is the unsteady diffusion equation

$$\frac{\partial c}{\partial t} = D\nabla^2 c(\boldsymbol{x}, t) \qquad \text{for } \boldsymbol{x} \in \{\Omega \setminus \partial\Omega\}\,,\ 0 < t \leqslant T\,, \tag{1}$$

where D denotes the scalar diffusion coefficient and ∇^2 is the Laplace operator. The initial concentration field is specified by

$$c(\boldsymbol{x}, t = 0) = c_0(\boldsymbol{x}) \qquad \boldsymbol{x} \in \Omega,\ t = 0\,.$$

As soluble proteins do not spontaneously cross the membrane the assumed boundary condition is the zero flux *Neumann* condition

$$\frac{\partial c}{\partial \boldsymbol{n}} = \nabla c(\boldsymbol{x}, t) \cdot \boldsymbol{n} = 0 \qquad \text{for } \boldsymbol{x} \in \partial\Omega,\ 0 < t \leqslant T\,,$$

where $\boldsymbol{n}$ is the outer unit normal on $\partial\Omega$, ∇c is the gradient of the concentration field c with respect to the location $\boldsymbol{x}$, and the dot denotes the scalar product of two vectors. If the value c rather than the flux is prescribed to be zero on the boundary, the boundary condition is called a zero value *Dirichlet* condition.

Particle Methods

Particle methods rely on the formulation of the quantities of interest as integral operators that are subsequently discretized using as quadrature points the locations of computational elements. The computational elements then can be viewed as *particles* carrying a physical quantity called *strength*. The particle attributes (strength and location) can be modified so as to satisfy the underlying governing equation. Following this procedure, a function c is discretized onto particles in three steps:

- *Step 1: Integral Representation.* Using the Dirac δ-function identity, the function c can be expressed as an integral operator

$$c(\boldsymbol{x}) = \int c(\boldsymbol{y})\,\delta(\boldsymbol{y} - \boldsymbol{x})\,d\boldsymbol{y} \qquad \text{for } \boldsymbol{x},\ \boldsymbol{y} \in \Omega\,.$$

The above integral can be discretized on a set of computational elements. Such a discretization does however not enable the recovery of the function values at locations other than those occupied by the particles. To circumvent this difficulty, the δ-function is replaced by a mollified approximation resulting in:

- *Step 2: Integral Mollification.*

$$c_\epsilon(\boldsymbol{x}) = \int c(\boldsymbol{y})\, \zeta_\epsilon(\boldsymbol{y} - \boldsymbol{x})\, d\boldsymbol{y}\,.$$

Note that

$$c_\epsilon(\boldsymbol{x}) = c(\boldsymbol{x}) + O(\epsilon^r)\,,$$

where r depends on the vanishing moments of the mollifying function ζ_ϵ. For positive symmetric functions, such as a Gaussian, $r = 2$.

- *Step 3: Mollified Integral Discretization.* The mollified integral is discretized over N particles using a quadrature rule

$$c_\epsilon^h(\boldsymbol{x}) = \sum_{p=1}^{N} \Gamma_p \zeta_\epsilon(\boldsymbol{x}_p - \boldsymbol{x})\,,$$

where the strength $\Gamma_p = \Gamma(\boldsymbol{x}_p)$ is an extensive property of the particles that depends on the particular quadrature rule. Here we use the rectangular rule setting the particle volumes $v_p = h^m$ and thus $\Gamma_p = c(\boldsymbol{x}_p)h^m$ where m is the space dimension and h is the inter-particle distance. Using this discretization we obtain

$$c_\epsilon^h(\boldsymbol{x}) = c_\epsilon(\boldsymbol{x}) + O\left(\frac{h}{\epsilon}\right)^s = c(\boldsymbol{x}) + O(\epsilon^r) + O\left(\frac{h}{\epsilon}\right)^s\,,$$

where s depends on the number of continuous derivatives of the mollifying function ζ_ϵ. For a Gaussian $s \to \infty$.

It is important to note that for the approximation to be consistent, it is required that the distance h between any two particles is always less than their mollified support ϵ, thus

$$\frac{h}{\epsilon} < 1\,.$$

See (4, 6) for further details on approximations of continuous functions by particles.

Particle Methods for Diffusion

The simulation of diffusion by particle methods can be formulated in the above mentioned framework. Solving the diffusion equation begins by expressing its solution in integral form. Without any boundary conditions this can be accomplished by considering the Green's function solution to the governing equation

$$c(\boldsymbol{x},t) = \int_{-\infty}^{\infty} G(\boldsymbol{x},\boldsymbol{y},t)c_0(\boldsymbol{y})\,d\boldsymbol{y}\,, \tag{2}$$

with Green's function being

$$G(\boldsymbol{x},\boldsymbol{y},t) = \frac{1}{(4\pi Dt)^{m/2}}\exp\left[-\frac{1}{4Dt}\sum_{i=1}^{m}(x_i-y_i)^2\right],$$

where $\exp[\cdot]$ stands for the exponential function and x_i means the i-th component of the vector $\boldsymbol{x}$.

The method of random walk

In the context of the random walk (3), the integral solution (Eq. 2) is interpreted probabilistically as follows: Place N randomly spaced particles at initial positions $\boldsymbol{x}_p^0$, $p = 1,\ldots,N$ and assign to each particle a strength of $\Gamma_p = h^m c_0(\boldsymbol{x}_p^0)$ where h is the inter-particle spacing. Let then the particles undergo a random walk by changing their positions at each time step n according to

$$\boldsymbol{x}_p^{n+1} = \boldsymbol{x}_p^n + \boldsymbol{\xi}_p^n\,,$$

where $\boldsymbol{\xi}_p^n$ are independent, identically distributed Gaussian random vectors with all components having mean 0 and variance $2mD\delta t$, where δt is the simulation time step size. The method is consistent since as we let the number N of particles go to infinity we observe that the expected distribution of the particle strength in space converges to the integral solution (Eq. 2). The random walk is however a stochastic method. This fact limits its convergence capabilities since the variance of the mean of N independent, identically distributed random variables is given by $1/\sqrt{N}$ times the individual variance of a single random variable (cf. benchmark case). Moreover, the solution deteriorates further with increasing diffusion constant since the variance of the random variables becomes larger.

The isotropic PSE method for infinite domains

Rather than discretizing Eq. 2 directly, the PSE method as introduced in (5) approximates the Laplace operator by an integral operator that allows consistent evaluation on the particle locations. This integral operator is found to be:

$$\nabla^2 c(\boldsymbol{x}) = \epsilon^{-2} \int \left(c(\boldsymbol{y}) - c(\boldsymbol{x})\right) \eta_\epsilon(\boldsymbol{y} - \boldsymbol{x})\, d\boldsymbol{y} + O\left(\epsilon^r\right) , \tag{3}$$

where $\eta_\epsilon(\boldsymbol{x}) = \epsilon^{-m}\eta(\boldsymbol{x}/\epsilon)$ is a kernel function in m dimensions that has to fulfill certain moment conditions (explicitly stated in (5) or (4)). An example of such a kernel function in $m = 1$ dimension is the Gaussian kernel given in Eq. 10. The approximation error of above operator is $O(\epsilon^r)$ with r being the order of the method (see (4) for a rigorous error treatment). Discretizing Eq. 3 using the rectangular quadrature rule with the particle locations $\boldsymbol{x}_p$ as quadrature points leads to:

$$\nabla^2_{\epsilon,h} c^h(\boldsymbol{x}^h_p) = \epsilon^{-2} \sum_{q \neq p} (\Gamma_q - \Gamma_p) \eta_\epsilon(\boldsymbol{x}_q - \boldsymbol{x}_p) , \tag{4}$$

where Γ_q and Γ_p are the particle strengths as defined earlier. The quadrature error is $O(h/\epsilon)^s$ where s is the number of continuous derivatives of the kernel function $\eta(\boldsymbol{x})$ and h is the inter-particle spacing. It is noteworthy that this operator is not the only possibility of discretizing the Laplacian onto particles. Compared to other deterministic diffusion schemes (see (4) for details), the PSE has however the big advantage of being conservative (i.e. exact conservation of the total strength in the system).

As outlined earlier, the approximation c^h_ϵ to the continuous concentration c at any location and time can be reconstructed from the values c^h_p at particle locations using:

$$c^h_\epsilon(\boldsymbol{x}, t) = \sum_p \Gamma_p(t) \zeta_\epsilon(\boldsymbol{x}_p(t) - \boldsymbol{x}) ,$$

where $\zeta_\epsilon(\boldsymbol{x}) = \epsilon^{-m}\zeta(\boldsymbol{x}/\epsilon)$ is the mollifier function that the particles "carry around". The final PSE scheme is easily obtained by inserting Eq. 4 into Eq. 1:

$$\frac{\partial c^h_p}{\partial t} = D\epsilon^{-2} \sum_{q \neq p} (\Gamma_q - \Gamma_p) \eta_\epsilon(\boldsymbol{x}^h_q - \boldsymbol{x}^h_p) \qquad \forall\, p \in \{1, \ldots, N\} . \tag{5}$$

This is an N-body problem as for each particle it involves a sum over all the other particles. However, since the kernel η_ϵ is chosen to be local, only the nearest neighbors of each particle significantly contribute to its sum. The simulations implement a Verlet list algorithm (12) for nearest neighbor search and interactions are only calculated between particles that are closer than a cut-off radius of $r_c = 3\epsilon$ resulting in a computational cost that scales linearly with the number of particles. It can be seen from Eq. 5, that in order to simulate diffusion, the strengths of all the particles change (i.e. they exchange mass) while their locations remain constant. This is in contrast to the method of random walk where the particle strengths are constant but their locations change. Having the particles at fixed locations has the convenient side-effect that all the geometry handling only needs to be done once when initializing the particles.

Extending the PSE for diffusion in complex geometries

The PSE algorithm as described above only applies to infinite domains. For diffusion in constrained geometries, the PSE needs to be modified to take into account the prescribed boundary conditions. For homogeneous boundary conditions in the case of flat (compared to the core size ϵ of the mollification kernel ζ_ϵ) boundaries a straightforward method consists of placing mirror particles in a r_c-neighborhood outside of the simulation domain. In the resulting method of images Eq. 3 becomes

$$\nabla^2 c(\boldsymbol{x}) = \epsilon^{-2} \int \left(c(\boldsymbol{y}) - c(\boldsymbol{x})\right) \left(\eta_\epsilon(\boldsymbol{y}-\boldsymbol{x}) \pm \eta_\epsilon(\boldsymbol{y}+\boldsymbol{x})\right) \, d\boldsymbol{y} + O(\epsilon^r) \tag{6}$$

and the method is represented as

$$\frac{\partial c_p^h}{\partial t} = D\epsilon^{-2} \sum_{q \neq p} (\Gamma_q - \Gamma_p) \left(\eta_\epsilon(\boldsymbol{x}_q - \boldsymbol{x}_p) \pm \eta_\epsilon(\boldsymbol{x}_q + \boldsymbol{x}_p)\right) \quad \forall\, p\,. \tag{7}$$

The positive sign between the two kernel functions applies for zero flux Neumann boundary conditions whereas the negative sign is to be taken in the case of zero value Dirichlet boundary conditions. The method of images is however restricted to the case of zero boundary values. For non-zero boundary values, the boundary conditions can be enforced by modifying the particle strengths in the vicinity of the boundary (7).

Benchmark case

The convergence properties of the PSE method and the method of random walk are illustrated on the problem of solving Eq. 1 on the one dimensional (i.e. $m = 1$) line $\Omega = [0, \infty)$ subject to the following initial and boundary conditions:

$$\begin{cases} c(x, t=0) = c_0(x) = xe^{-x^2} & x \in [0,\infty),\ t = 0 \\ c(x=0, t) = 0 & x = 0,\ 0 < t \leqslant T\,. \end{cases} \tag{8}$$

Using the method of images, the exact solution of this problem is found to be

$$c^{ex}(x,t) = \frac{x}{(1+4Dt)^{3/2}} e^{-x^2/(1+4Dt)}\,. \tag{9}$$

Both random walk and PSE simulations of this test case are performed with a varying number of particles to study their spatial convergence behavior. In order to meet the boundary condition at $x = 0$ the random walk solution is calculated for $2N$ particles initially uniformly placed on the line $[-X, X]$ such that N particles have locations $x_p^0 \geqslant 0$. The domain boundary X has to be chosen large enough such that $c(X, t) < \varepsilon$ (with ε being the machine epsilon of the computer) for the whole duration of the simulation. Each of the $2N$ particles is assigned a strength of $\Gamma_p = X c_o(|x_p^0|)/N$. Then the particles undergo a one-dimensional random walk. To recover the solution at a later time step n, the domain of solution $[0, X]$ is subdivided into

M disjoint intervals of size $\delta x = X/M$ and the particles are sampled in these intervals as follows: each interval $j = 1, \ldots, M$ is assigned the sum of the strengths of all the particles having positions between $(j - 3/2)\delta x$ and $(j - 1/2)\delta x$, thus

$$c^{RW}((j-1)\delta x, n\delta t) = \frac{1}{\delta x} \sum_p \left\{ \Gamma_p : (j-1)\delta x < x_p^n + \frac{1}{2}\delta x \leqslant j\delta x \right\}$$

for $j = 1, \ldots, M$.

For the PSE, the method as given by Eq. 5 is implemented. The boundary condition is treated in the same way as for the random walk, i.e. the interval $[-X, X]$ is covered with $2N$ uniformly spaced particles at locations x_p, $p = 1, \ldots, 2N$. This is the method of images since it is equivalent to using mirror kernels as in Eq. 7. The inter-particle spacing is $h = X/(N-1)$. Initially each particle is assigned a strength of $\Gamma_p = X c_o(|x_p|)/N$, as in the random walk case. The PSE scheme (Eq. 5) is discretized in time using the explicit Euler method. The strengths of the particles are therefore updated in each time step $n = 0, 1, 2 \ldots$ as follows:

$$\Gamma_p^{n+1} = \Gamma_p^n + \frac{hD\delta t}{\epsilon^2} \sum_{q \neq p} \left(\Gamma_q^n - \Gamma_p^n \right) \eta_\epsilon(x_q - x_p) \qquad \forall\, p \in \{1, \ldots, 2N\} \; .$$

For η_ϵ the following 2^{nd} order Gaussian kernel is used:

$$\eta_\epsilon(x) = \frac{1}{2\epsilon\sqrt{\pi}} e^{-x^2/4\epsilon^2} \; , \tag{10}$$

which fulfills all the requirements stated in (5) in 1D at order $r = 2$. The concentration values at particle locations x_p and simulation time points $t_n = n\delta t$ are recovered as

$$c^{PSE}(x_p, t^n) = \Gamma_p^n \cdot N/X \; .$$

Supplementary Fig. 2 shows the random walk and PSE solutions at a final time of $T = 10$ time units for $N = 50$ particles and a diffusion constant of $D = 10^{-4}$ (length units)^2/time unit.

The accuracy of the simulations for different numbers of particles is assessed by computing the final RMS error

$$E_{\text{RMS}} = \left[\frac{1}{N} \sum_{p=0}^{N} \left(c^{ex}(x_p, T) - c(x_p, T) \right)^2 \right]^{1/2} \tag{11}$$

for each N. The resulting convergence curves are shown in a double logarithmic plot in supplementary Fig. 3.

For the random walk one observes the characteristic slow convergence of $O(1/\sqrt{N})$ as it has been estimated in (8). For the PSE, a convergence of $O(1/N^2)$ is observed which is in agreement with the employed 2^{nd} order kernel function. Below an error of 10^{-6} machine precision is reached. It can be seen that the RMS error of the PSE simulations is several orders of

magnitude lower than the one of the random walk simulations for the same number of particles. Using only 100 particles, the PSE is already close to machine precision. It is evident from these results that to get a reasonable accuracy using the method of random walk, large numbers of particles are necessary.

To extend the validation, a 3D benchmark case in a simple fluorescence recovery setting where the exact analytic solution can be calculated is also considered (9). The PSE is compared to the exact solution as well as to a finite difference and a random walk solution of the same problem. The PSE consistently has an RMS error at least an order of magnitude below the other methods while being more than an order of magnitude faster than a random walk simulation of the same accuracy.

Simulating diffusion in the lumen of the Endoplasmic Reticulum

The method of PSE is applied to the simulation of fluorescence recovery in the Endoplasmic Reticulum (ER). Hereby, the diffusive motion of a fluorescently labeled soluble protein in the ER lumen is simulated and the total fluorescence intensity inside an originally bleached region B is monitored over time. We assume the species of interest to diffuse normally (i.e. no anomalous diffusion) and freely within the confines of the ER lumen Ω. In the following, the FRAP value at time $t_n = n\delta t$ is defined as

$$F(t_n) = \frac{1}{N_B} \sum_{p \in B} c_p^h(t_n)\,, \tag{12}$$

where N_B is the total number of particles inside the initialy bleached volume B and $c_p^h(t_n)$ is the PSE solution of the concentration field. **In order to focus on the influence of organelle geometry, we use the idealized initial condition**

$$c_0(\boldsymbol{x}) = \begin{cases} 0 & \text{if } \boldsymbol{x} \in \{\Omega \cap B\} \\ k & \text{if } \boldsymbol{x} \in \{\Omega \setminus B\}\,. \end{cases} \tag{13}$$

Using more realistic initial conditions (1, 13) would leave all conclusions unchanged as their effects would equally apply to all simulations. The initially bleached volume B is taken to be the square cylinder defined by:

$$B = [p,q] \times [r,s] \times [0, L_z] \qquad \begin{cases} 0 \leqslant p < q \leqslant L_x \\ 0 \leqslant r < s \leqslant L_y\,, \end{cases} \tag{14}$$

with (L_x, L_y, L_z) being the extent of the ER in all spatial directions. Without loss of generality, the constant initial concentration outside the bleached area is chosen to be $k = 1$ as this simply corresponds to normalizing the FRAP curves with respect to the pre-bleach value. The

assumption of a homogeneous initial concentration distribution outside the bleached area seems feasible due to the following facts:

1. After transfection, the cells are incubated for at least 12 hours. During this time they express the green fluorescent protein which is assumed to freely diffuse in the ER lumen and to fill it completely. Experiments show that a protein can easily move across the whole ER in about 20 s. Therefore a homogeneous distribution inside the ER is assumed after 12 hours.

2. The experimenter chooses "healthy" cells, i.e. cells which exhibit a more or less homogeneous fluorescence inside the ER.

More realistic initial conditions (1, 13) can readily be satisfied by accordingly setting the initial strengths of the particles.

The geometric domains Ω for the simulations are reconstructed samples of real ER structures from VERO cells as described in the methods section of the main text. The shape of a particular ER sample is captured by a stack of serial sections using confocal fluorescence light microscopy. These stacks are then used to reconstruct the surface of the ERs in three dimensions in a computer. The reconstructed surfaces are represented and stored as triangulations (10) and checked to enclose a connected space with no holes or intersections in its surface. Figure 2 of the main manuscript shows a sample outcome of such a reconstruction procedure.

All PSE simulations are run for the same value of the diffusion constant $D = 3 \cdot 10^{-5}\, b^2/\delta t$ **(scaled with the lateral edge length** b **of the bleached region and the simulation time step** δt**) in order to be able to study the influences of geometry. All simulations are run to a final time of** $T = 2000\, \delta t$**.** The PSE kernel support is $\epsilon = 2.222$ for all runs.

Since the bleached areas of the different ER samples contain different numbers of particles and the total number of particles also varies among samples, the different FRAP curves will have different asymptotic levels as $t \to \infty$. Moreover, the FRAP curves will normally not recover to 1 even if the protein is fully mobile. This is due to the zero flux boundary condition and the fact that the total mass in the domain is conserved. In order to be able to compare the FRAP curves of the simulation runs amongst each other, they are normalized by their respective steady-state value c_∞. Therefore, they all asymptotically recover to 1.0 leaving the different geometries as the only source of variations. Initially, the total mass in the system is given by

$$m_t = \sum_{p=1}^{N} h^m c_p^h = h^m (N - N_B)\,,$$

where N_B is the number of particles inside the bleached area. The latter equality makes use of the initial condition as given by Eq. 13 and the choice $k = 1$. The asymptotic value of the concentration is given by homogeneously distributing this mass among all the particles, thus

$$c_\infty = \frac{m_t}{Nh^m} = \frac{N - N_B}{N}\,. \tag{15}$$

Figure 4a of the main text shows the resulting normalized FRAP curves $F(t)/c_\infty$ for 4 different ER samples. As expected they differ due to geometry influences as all simulations have been done using the same diffusion constant. The recovery half-times of the curves vary within the interval $[5.7, 14.2]$, introducing an uncertainty of a factor of at least 2.5. Main text figure 3 shows snapshots of the concentration distribution in a sample ER shape at simulation times 0.01, 0.25, 1.5 and 3.0. Only the part of the ER around the bleached volume is shown.

Error analysis of 3D reconstruction and influence of the microscope's optical anisotropy

In order to determine the optimal threshold (intensity iso-value) for the 3D reconstruction of the z-stacks, the reconstruction process is analyzed using synthetic geometries. For synthetic geometries, we know what the correct outcome should look like. Artificial random networks of tubules are created in the computer. The networks is generated on a lattice of m points.

An example with $m = 20 \times 20 \times 3$ is shown in supplementary Fig. 4. These geometries are then convolved with a model of the (anisotropic) point spread function of a confocal microscope. The lateral resolution of the microscope is expressed as

$$R = \frac{\lambda}{2NA}\,,$$

with λ the wavelength of light and NA the numerical aperture of the objective lens. The axial resolution is defined as the distance between the nearest and farthest planes simultaneously in focus and, according to (11),

$$d = \frac{3n\lambda}{2NA^2}\,,$$

where n is the refractive index of the medium. The ratio d/R is called *optical anisotropy* of the microscope and it varies between about 1.6 and 5 for commercial confocal microscopes. The point spread function according to (14) is modeled in each space direction as

$$P(r) = \left(2\frac{J_1(ar)}{r}\right)^2$$

with

$$a = \frac{2\pi \cdot NA}{\lambda}$$

and J_1 the Bessel function of first kind. For the axial direction: $a_x = aR/d$. The values used for our work are $\lambda = 510\,\mathrm{nm}$, $NA = 1.4$, and $n = 1$.

Successive convolution with $P(r)$ in all three spatial directions yields a simulated z-stack of plane images as shown in supplementary Fig. 5. Each pixel in these images is replaced by a Poisson-distributed random number with an expectation value equal to the original pixel value. This realistically simulates the effects of CCD camera shot pixel noise (2). The section images are normalized such that all intensity values are between 0 and 255.

The so obtained images are reconstructed using Imaris 3 (BitPlane, Inc.) and the resulting reconstructed volumes compared the the original ones. The deviation is measured as the relative number of voxels that are not correctly reconstructed (i.e. they are missing in the reconstructed geometry, but are present in the original one, or vice versa). Supplementary Fig. 6 shows the resulting total reconstruction errors for various thresholds and optical anisotropies for a test geometry with an expected number of 2 connections per branching point, $0.15\,\mu$m tubule radius, and an average distance of $1\,\mu$m between tubules. **This corresponds to a volume-filling ratio of 0.3. The ER fills on average 1/3 of the bounding volume and is thus of comparable density.** Similar studies are also done for larger tubules (radius $0.25\,\mu$m) and a lower connection density (avg. 1 connection per braching point). A total of 4 different geometries is analyzed for 5 different anisotropy values (1, 2, 3, 4, 6, 8) each and a wide range of thresholds. The corresponding plots are not shown as they are very similar to the one in supplementary Fig. 6 and lead to the same conclusions.

We also determine the largest threshold for which the reconstructed network geometry is still connected (i.e. in one piece). It turns out that the optimal threshold is close to or larger than this limit for all anisotropies larger than 1 and all geometries studied. For the experimental ER samples we thus always use the largest possible threshold which yields a connected ER reconstruction, since the most important objective toward realistic computer simulations is to preserve the topology of the organelle. The anisotropy of the particular microscope used is about 2.14, the optimal threshold can thus be expected to be reasonably close to the largest possible one.

For the sensitivity of the reconstruction outcome with respect to the threshold setting, we find that varying the threshold by $\pm 10\%$ around the optimum changes the reconstruction error by $+4 \ldots 8\%$ for anisotropies of 2 and 3. Using above-mentioned rule of thumb, such large threshold deviations will however never occur.

Chosing the reconstruction threshold as outlined preserves the topology of the tubular network. The reconstruction errors will however still cause the tubules to appear thicker or thinner than they are in reality. The error in the predicted diffusion speed is directly proportional to this size error. For an anisotropy of 2, the total relative recontstruction error is 28%, composed of 16% missing voxels and 12% excess voxels. A tubule thus appears on average 4% thinner than it actually is. This translates into a 4% error in the predicted diffusion constant, which increases to 9% for an anisotropy of 3. Compared to the various experimental uncertainties, these errors constitute no significant reservation.

References

[1] Braga, J., J. M. P. Desterro, and M. Carmo-Fonseca. 2004. Intracellular macromolecular mobility measured by fluorescence recovery after photobleaching with confocal laser scanning microscopes. *Molec. Biol. Cell*. 15:4749–4760.

[2] Cheezum, M. K., W. F. Walker, and W. H. Guilford. 2001. Quantitative comparison of algorithms for tracking single fluorescent particles. *Biophys. J.* 81:2378–2388.

[3] Chorin, A. J. 1973. Numerical study of slightly viscous flow. *J. Fluid Mech.* 57:785–796.

[4] Cottet, G.-H., and P. Koumoutsakos. 2000. Vortex Methods – Theory and Practice. Cambridge University Press, New York.

[5] Degond, P., and S. Mas-Gallic. 1989. The weighted particle method for convection-diffusion equations. part 1: The case of an isotropic viscosity. *Math. Comput.* 53:485–507. Oct.

[6] Koumoutsakos, P. 2005. Multiscale flow simulations using particles. *Annu. Rev. Fluid Mech.* 37:457–487.

[7] Koumoutsakos, P., A. Leonard, and F. Pépin. 1994. Boundary conditions for viscous vortex methods. *J. Comput. Phys.* 113:52–61.

[8] Milizzano, F., and P. G. Saffman. 1977. The calculation of large reynolds number two-dimensional flow using discrete vortices with random walk. *J. Comput. Phys.* 23:380–392.

[9] Sbalzarini, I. F. 2002. Diffusion in the endoplasmic reticulum – theoretical foundation, computer simulations, models. Diploma thesis. Http://e-collection.ethbib.ethz.ch/cgi-bin/show.pl?type=dipl&nr=16.

[10] Schumaker, L. L. 1987. Triangulation methods. *In* Multivariate Approximation. Annalen der Physik. 219–232.

[11] Spring, K. R., and M. W. Davidson. ???? Depth of field and depth of focus. Technical report. Www.microscopyu.com/articles/formulas/formulasfileddepth.html.

[12] Verlet, L. 1967. Computer experiments on classical fluids. I. Thermodynamical properties of Lennard-Jones molecules. *Phys. Rev.* 159:98–103.

[13] Weiss, M. 2004. Challenges and artifacts in quantitative photobleaching experiments. *Traffic*. 5:662–671.

[14] Young, I. T. 1996. Quantitative microscopy. *IEEE Engineering in medicine and biology*. :59–66.

Supplementary figure legends

Supplementary figure 1

a: Simulated FRAP curve compared to experimental measurement data.

Random walk simulation of fluorescence recovery curves in 2D and 3D. Both a 2D simulation on the square plane $[0, L] \times [0, L]$ (solid) and a 3D simulation in the cubic box $[0, L] \times [0, L] \times [0, L]$ (dashed) using the same computational diffusion constant $D = 1.56 \cdot 10^{-4}\, L^2/\delta t$ and zero flux boundary conditions are performed. 10^5 particles are used for both simulations. Each curve is averaged from 5 computations using different random number series. The asymptotic level of 0.9375 is shown as a dotted line.

b: The influence of confinement: Diffusion in a cube versus diffusion in the ER.

Both simulations are made using the same diffusion constant. Depending on which ER geometry sample is used the recovery half-time for the ER case (solid) is 1.8–4.2 times the one of the cube (dashed). The average volume-filling coefficient of the ER is about 0.33. Both curves are normalized by their respective asymptotic level to allow geometric comparison.

Supplementary figure 2

Comparison of random walk and PSE solutions for the benchmark case. The random walk (a) and PSE (b) solutions of the benchmark case at time $T = 10$ are shown (*circles*) along with the exact solution (*solid line*). For both methods $N = 50$ particles, a time step of $\delta t = 0.1$, $D = 10^{-4}$ and $X = 4$ are used. The random walk solution is sampled in $M = 20$ intervals of $\delta x = 0.2$. For the PSE a core size of $\epsilon = h$ is used.

Supplementary figure 3

Convergence curves for random walk and PSE. The RMS error versus the number of particles for the random walk (*triangles*) and the PSE (*circles*) solutions of benchmark case at time $T = 10$ are shown. For both methods $N = 50$ particles, a time step of $\delta t = 0.1$, $D = 10^{-4}$ and $X = 4$ are used. The random walk solution is sampled in $M = 20$ intervals of $\delta x = 0.2$ and for the PSE a core size of $\epsilon = h$ is used. The RMS error is calculated according to Eq. 11. We use single machine precision and thus expect the curves to level off below an error of about 10^{-6}.

Supplementary figure 4

Example of an artificial tubular network geometry used to assess the quality of 3D reconstruction. The random network is generated on a $20 \times 20 \times 3$ lattice with an average of 2 tubules being connected in each grid point. The radius of the tubules is $0.15\,\mu$m, the distance between two

grid points is $1\,\mu$m. (a) shows the full network, imaged at an anisotropy of 3 and reconstructed with a threshold of 50. (b) shows a $4 \times 4 \times 3$ subset imaged at anisotropy 1 and reconstructed with a threshold of 110.

Supplementary figure 5

Artificial z-stack created from the sample geometry of supplementary Fig. 4b. After convolving the geometry to model the effect of confocal imaging with an anisotropy of 4, 15 serial section images at an axial distance of $0.2\,\mu$m are taken. The same geometry is also tested using up to 53 sections (images not shown). Progressing from left to right and top to bottom, the simulated confocal plane moves from the bottom of the object to its top.

Supplementary figure 6

Relative reconstruction errors for the sample geometry of supplementary Fig. 4b and different optical anisotropies and reconstruction thresholds. The x axis shows the pixel intensity iso-value value used for the 3D reconstruction. The intensity values in the images are between 0 and 255. The y axis shows the relative reconstruction error, which is the number of incorrect voxels in the reconstructed volume divided by the total number of voxels in the original volume. Lines are shown for various anisotropies. The squares mark the largest threshold for which a connected reconstruction resulted. For the idealized case of anisotropy 1, the reconstruction is always connected.

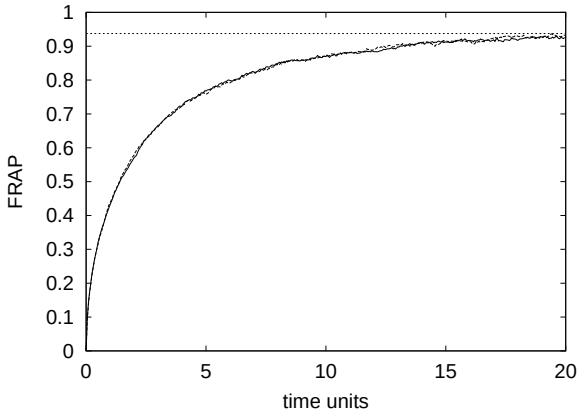

a

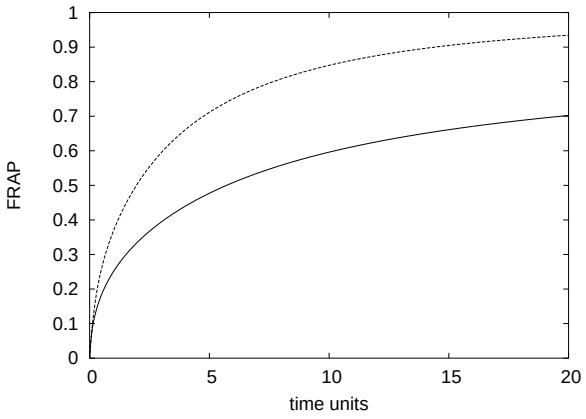

b

Figure 1: (Supplementary Material, Sbalzarini et al.)

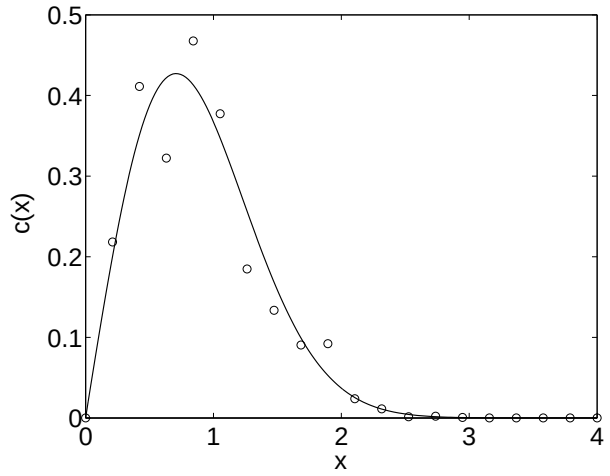

a: Random Walk

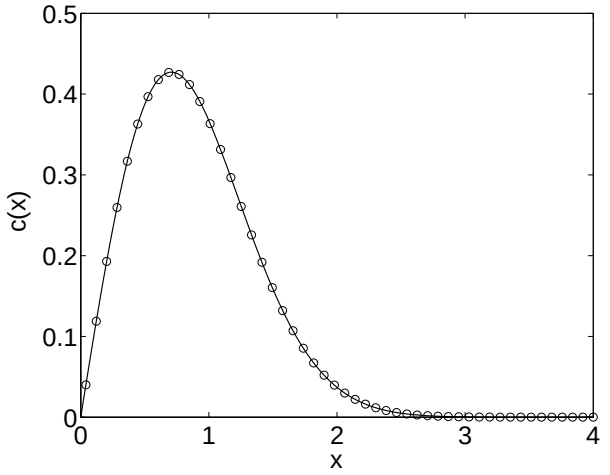

b: PSE

Figure 2: Supplementary Material, Sbalzarini et. al.

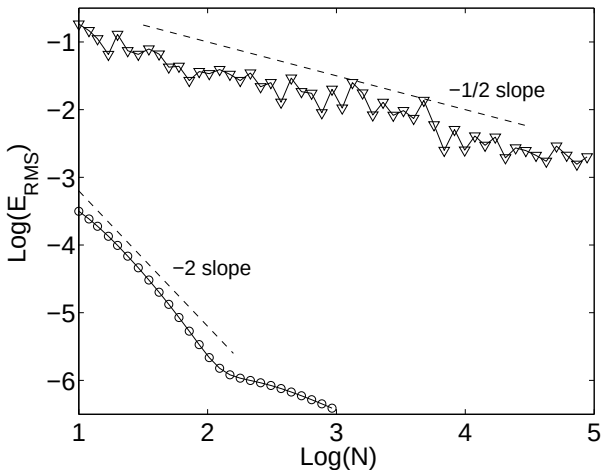

Figure 3: Supplementary Material, Sbalzarini et. al.

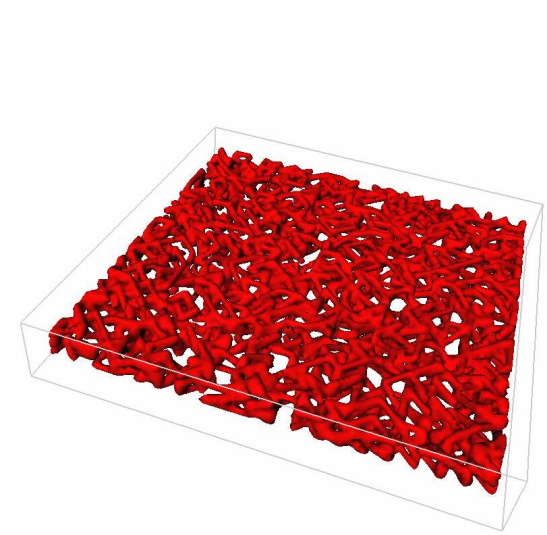

a: Whole network, anisotropy 3

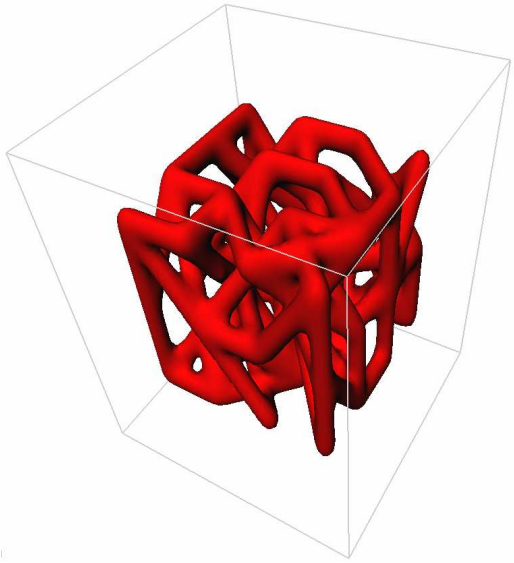

b: $4 \times 4 \times 3$ closeup, anisotropy 1

Figure 4: Supplementary Material, Sbalzarini et. al.

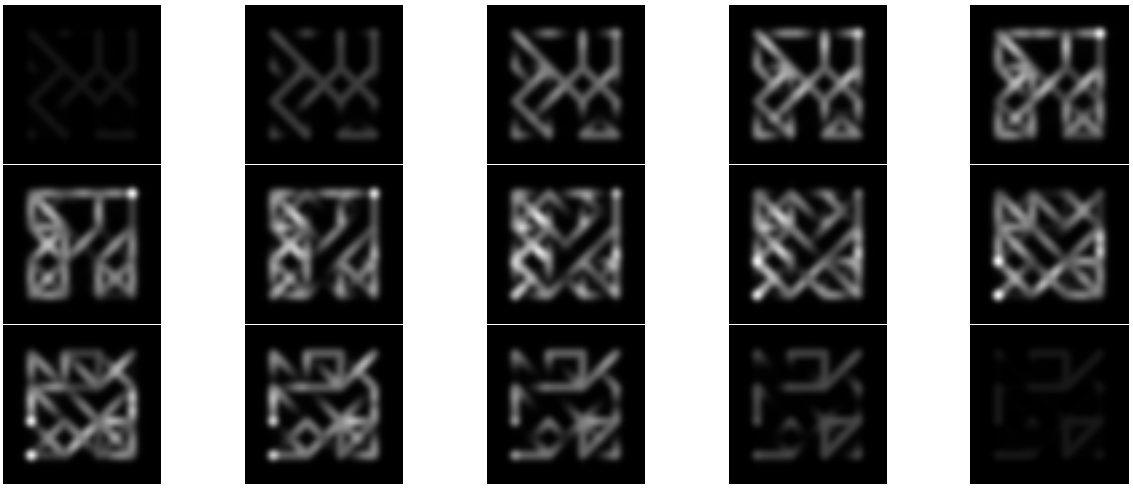

Figure 5: Supplementary Material, Sbalzarini et. al.

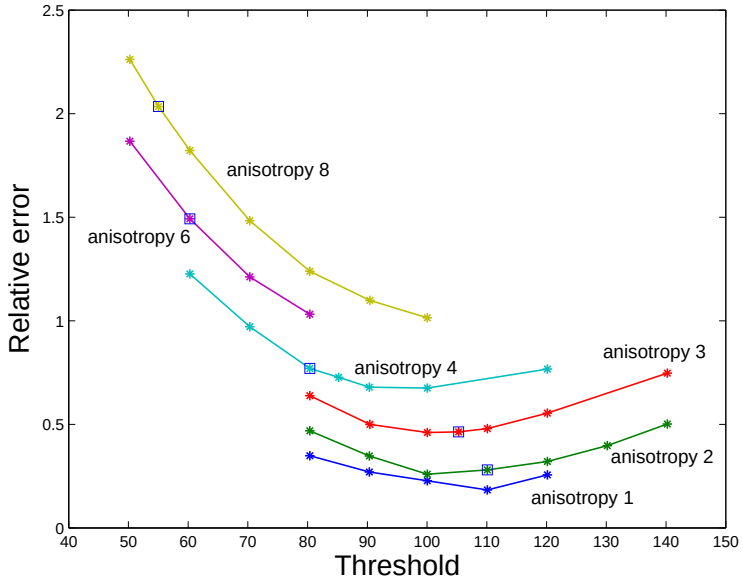

Figure 6: Supplementary Material, Sbalzarini et. al.